where ω_S is Strouhal shedding frequency; the constants β_L^+, γ_L^+, η_L^+, E_L^+, and D_L^+ are given a superscript (+) to characterize the periodic time-varying regime. The decay regime of the periodic time-varying equilibrium state is simply modeled by a damped oscillator:

$$\ddot{C}_{L_u} - \omega_S \beta_L^- \dot{C}_{L_u} + \omega_S^2 C_{L_u} = 0 \tag{4}$$

where the constant β_L^- is negative. The values of the seven constants ω_S, β_L^+, γ_L^+, η_L^+, E_L^+, D_L^+, and β_L^- can be evaluated from two-dimensional unsteady experiments in the stall regime of the flow. There are no equivalent equations to Eqs. (3) and (4) in other dynamic stall models. The present modeling lies on the existence of ω_S.

Discussion

The case study no. 596 of S1–Modane experiment is treated in this Note. This case corresponds to a high speed ($\mu = 0.40$) and to high loading (thrust coefficient $C_T/\sigma = 0.147$), and therefore, blade stall is present on the retreating side. The experimental measurements of the normalized normal force coefficient at two spanwise locations $r/R = 0.825$ and 0.50, are shown in Fig. 1, with calculated values, based on quasistatic two-dimensional aerodynamics and on the "Hopf bifurcation stall model," respectively.

Undulatory behavior is clearly shown on the blade retreating side, i.e., in the azimuthal range of 210–360 deg, for the normalized normal force coefficient at section $r/R = 0.825$. Other published experimental results[8,9] also exhibit such features. This undulatory behavior is a clear manifestation of multiple vortex-shedding phenomena. The amplitude of the oscillations of the modeled results appears smaller than that of the experimental results. The higher amplitude-observed experimentally is probably due to plunging effects that are not correctly taken into account by the dynamic stall model. For the inboard section $r/R = 0.50$, the amplitude of the oscillations is reduced, and this trend is correctly predicted by the model.

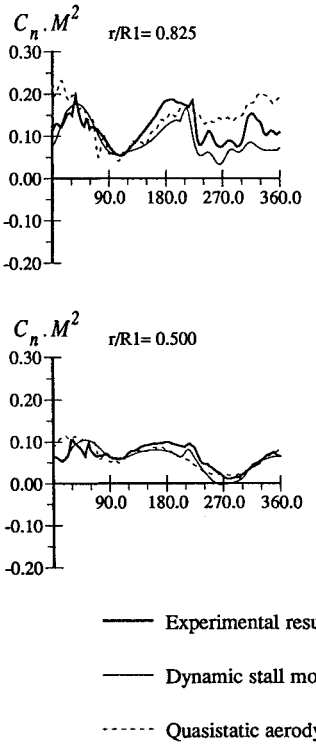

Fig. 1 Experimental and calculated results of the normalized force coefficient $C_n.M^2$ for study no. 596 of the S1-Modane wind-tunnel experiment.

As long as the amplitudes of the oscillations of the normal force coefficient are not negligible, multiple vortex-shedding phenomena cannot be ignored. The recent results on the UH-60A rotor[9] indicate that the amplitudes of the oscillations of section lift and pitching moment coefficients attain half the maximum of these values, respectively, for high thrust coefficient and a speed of $\mu = 0.24$. The results are very promising and the first author will now integrate the Hopf bifurcation dynamic stall model into an aeroelastic rotor code more elaborate than the one used here.

Acknowledgment

This study was funded by Direction des Recherches Etudes et Techniques.

References

[1]Ham, N. H., and Young, M. I., "Torsional Oscillation of Helicopter Blades Due to Stall," *Journal of Aircraft*, Vol. 3, No. 3, 1966, pp. 218–224.

[2]Young, W. H., and Hoad, D. R., "Comparison of Two Flow Surveys Above Stalled Wings," AIAA Paper 79-0147, 1979.

[3]Panda, J., and Zaman, K. B. M. Q., "Experimental Investigation of the Flowfield of an Oscillating Airfoil," NASA TM 105675, 1992.

[4]Truong, V. K., "Modèle de Décrochage 2-D Basé sur la Notion de Bifurcation de Hopf," *La Recherche Aérospatiale*, Vol. 4, 1993, pp. 55–65.

[5]Truong, V. K., "A 2-D Dynamic Stall Model Based on a Hopf Bifurcation," *Nineteenth European Rotorcraft Forum*, Paper C23, Cernobbio (Como), Italy, Sept. 1993.

[6]Tourjansky, N., and Szechenyi, E., "The Measurement of Blade Deflections," *Eighteenth European Rotorcraft Forum*, Paper E10, Avignon, France, Sept. 1992.

[7]Meijer-Drees, J., "A Theory of Air Flow Through Rotors and Its Application to Some Helicopter Problems," *Journal of the Helicopter Association of Great Britain*, Vol. 3, No. 2, 1949.

[8]McCroskey, W. J., and Fisher, R. K., "Detailed Aerodynamic Measurements on a Model Rotor in the Blade Stall Regime," *Journal of the American Helicopter Society*, Vol. 17, No. 1, 1972, pp. 20–30.

[9]Coleman, C. P., and Bousman, W. G., "Aerodynamic Limitations of the UH-60A Rotor," *American Helicopter Society Aeromechanics Specialists Conference*," Paper 8.5, CA, Jan. 1994.

Effects of Large Blockage in Wind-Tunnel Testing

Joseph Katz* and Robert Walters†
San Diego State University, San Diego, California 92182-0183

Introduction

WIND tunnels play an integral role in the aerodynamic development and refinement of virtually all airplanes and of numerous ground vehicles. Their advantage lies in the ability to generate a variety of conditions in terms of airspeed, angles of attack, and sideslip in a well-controlled environment. Test conditions are independent of atmospheric changes

Received Nov. 28, 1994; presented as Paper 95-0438 at the AIAA 33rd Aerospace Sciences Meeting and Exhibit, Reno, NV, Jan. 9–12, 1995; revision received Feb. 27, 1995; accepted for publication March 1, 1995.

*Professor, Department of Aerospace Engineering and Engineering Mechanics. Associate Fellow AIAA.

†Graduate Student, Department of Aerospace Engineering and Engineering Mechanics. Member AIAA.

and testing equipment is abundant and stationary, compared to some of the limitations during a flight test of an instrumented airplane. However, the fact that a model is being confined into a limited-size environment brings to light the first and most important conflict. One side of this conflict emerges from the need to reduce the operating costs of the testing facility. This requirement translates to a reduction in test-section size and drive power. In addition, as the wind-tunnel size increases, environmental difficulties may arise and some full-scale facilities must be placed in isolated research centers, at a safe distance from residential areas. The other side of the conflict is rooted in the need to increase model size to facilitate accessibility, while at the same time keep tunnel boundaries "sufficiently" far from the model. Furthermore, circumstances may occasionally require the testing of models that are larger than intended by the designers of a particular facility. And there always must be a compromise between model designers wishing to test the largest possible model and the available wind-tunnel facility with an existing test section.

As the distance between a model and the solid walls of a closed-test-section wind tunnel is reduced, several effects altering the measured data take place. One of the most obvious effects is the increase in airspeed in the narrowed passage between the model and the walls, which increases the aerodynamic coefficients. Another, quite important effect, is the interaction between the walls and lifting surfaces, resulting in reflections similar to ground effect. As a result of these and other test-section-wall effects, numerous semiempirical corrections were developed[1-3] and the test section to model frontal area ratio was limited (e.g., to less than 7.5%, in Ref. 2 p. 371). As computational methods matured, correction methods based on combining the results of flow computations over simple shapes with the measurement of wall-pressure signature were proposed. This approach (as in Refs. 4 and 5) allows the fine tuning of the correction technique to fit the unique geometry of a particular experiment. Another method is based on numerically modeling the detailed geometry of both the test section and the model, as proposed in Refs. 6 and 7. In those references, ideal flow models were used, which are quite effective for attached flow cases, and then both lift-reflection and blockage effects can be estimated (but not wake blockage or buoyancy).

Most wind-tunnel corrections are based on the assumption that test section blockage is usually less than 7.5%, as suggested in Ref. 2. This study, therefore, is aimed at generating information on the effects of blockage ratios larger than 7% (up to 20%), so that the changes in the aerodynamic coefficients under these extreme conditions can be estimated. Furthermore, such data can be used to validate numerical tools used as complementary tools in wind-tunnel testing and for comparison with various corrections applied to the measured experimental data. Two generic models were selected for this investigation, such that the first represents bluff-body flows and the second relates to the interaction between lifting wings and the walls in an attached flow environment. The longitudinal pressure signature along the wind-tunnel ceiling centerline was also measured, so that this additional information can be used to compare experimental results with numerical computations.

Experimental Setup

The wind tunnel used for the experiments is a closed-return-type with test-section dimensions of 0.81 m height and 1.15 m width. (Because of the slanted corners the actual cross-sectional area is $S = 0.9$ m^2.) Test-section airspeed varied between 25–65 m/s so that the Reynolds number, based on the body's length (or airfoil's chord) was about 1.4×10^6. The shapes of the two basic configurations and the method of their mounting in the wind-tunnel test section are depicted in Fig. 1. The first group of models (shown in the upper part of Fig. 1) represents a bluff body that consists of a hemispheric nose section attached to a cylinder, and held via a rear sting in the test section. The second basic shape was a rectangular wing, spanning the whole test section, and using a NACA 64_2-415 airfoil section. Four different, but similar models were constructed for each case (a total of eight models), creating test-section blockage in the range from 5 to 20%. The angle of attack of the wing models could be varied during the experiment by the rear strut, but the orientation of the cylindrical models was fixed, parallel to the freestream direction.

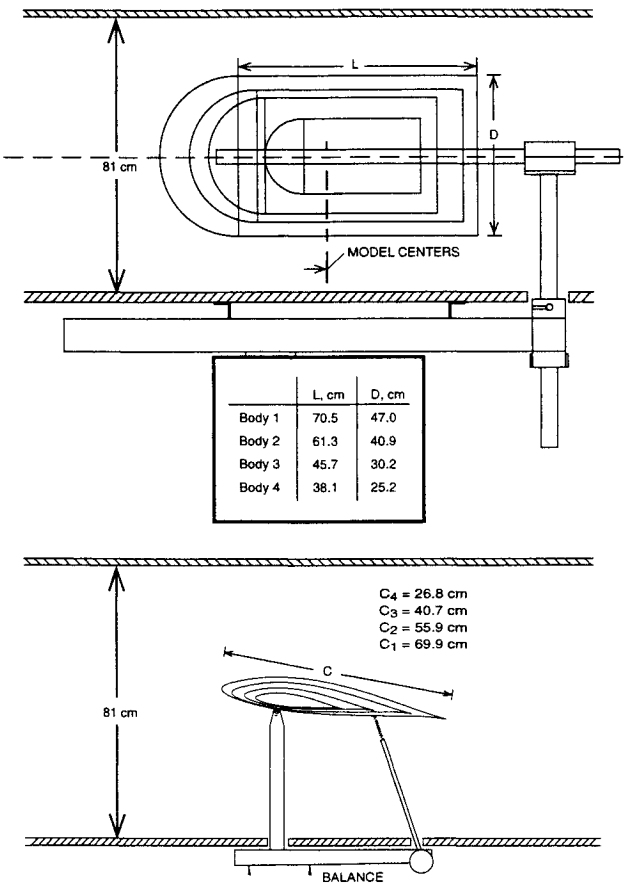

Fig. 1 Schematic description of the four bluff-body and four wing models, as mounted in the wind-tunnel test section.

Results

The aerodynamic data obtained from the wind-tunnel experiments included the six-component balance measurements and the pressure coefficient signatures along the test-section ceiling. For brevity though, only the ceiling pressure distribution and the drag coefficient data will be presented for the bluff bodies. More information about this experiment can be found in Ref. 8. The pressure distribution, as measured on the test-section ceiling, is shown in Fig. 2 for the four cylindrical bodies (the x coordinate is nondimensionalized by the largest cylinder length L_1). This data indicates that the airspeed increases ahead of the body's leading edge ($x/L_1 = 0$) and the maximum speed (or minimum C_p) is reached behind the junction between the hemisphere and the cylindrical aft body. The two most backward points on each curve in Fig. 2 show an increase in the suction peak toward the end of the body. This is partially due to the flow turning inward behind the bluff body and partially because of the time-dependent wake flow (but the static pressure equipment is recording the average pressure coefficient only). The fact that the pressure coefficient does not recover to a value near $C_p = 0$ behind the body indicates that the wake creates a blockage effect

Table 1 Variation of the drag coefficient with increasing test-section blockage

Body no.	Blockage, %	C_D, uncorrected
1	19.5	0.54
2	14.6	0.40
3	8.0	0.31
4	5.6	0.30

Note: Drag coefficient is based on model frontal area and maximum uncertainty in C_D is ± 0.01.

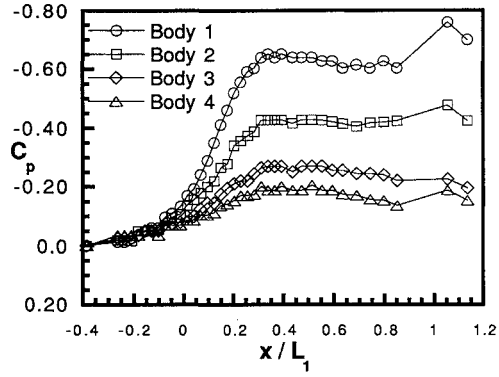

Fig. 2 Variation of the measured pressure coefficient along the test section ceiling for the four cylindrical bodies. Body 1 is the largest and body 4 is the smallest (maximum uncertainty in C_p is ± 0.03).

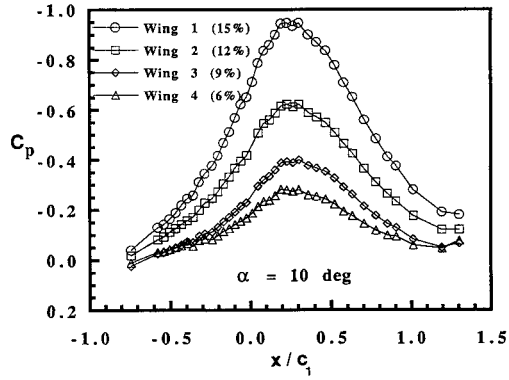

Fig. 3 Comparison of the pressure distribution along the centerline of the test section ceiling for the four wings at $\alpha = 10$ deg (maximum uncertainty in C_p is ± 0.03).

comparable to a solid body. Thus, the overall large variation of the static pressure along the wind-tunnel ceiling, especially for the larger body, indicates that the solid walls considerably affect the flowfield. As model size and the corresponding blockage increases, the magnitude of this pressure signature increases as well. In case of the largest body, e.g., the data indicate that the velocity near the wall is about 30% faster than the freestream velocity. This blockage effect, of course, causes a corresponding increase in the aerodynamic coefficients that can be demonstrated by observing the experimental drag results for the four bluff bodies (Table 1). This data clearly indicates the rapid increase in the uncorrected drag coefficient, with increasing blockage ratio, which is defined here as the model to test-section frontal area ratio.

The test program of the four wings when compared with the test program of the bluff bodies had an additional variable; the angle of attack. This increased the volume of the relevant experimental data, and more information on this part of the experiments can be found in Ref. 8. The effect of model size on the ceiling pressure distribution can be demonstrated by plotting the experimental data for a fixed angle of attack (e.g., $\alpha = 10$ deg) for all four wings, as shown in Fig. 3. At this angle, the blockage for all wings is quite large, but the flow

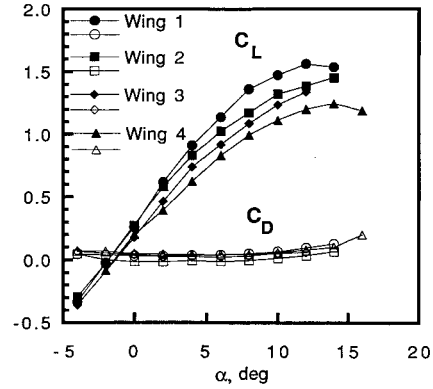

Fig. 4 Lift and drag coefficient variation for the four wing models. Wing 1 is the largest and wing 4 is the smallest (maximum uncertainty in C_L is ± 0.01, and in C_D it is ± 0.01).

is still attached. The extremum in the ceiling-pressure distribution in Fig. 3 takes place behind the wing's leading edge and increases with wing size and angle of attack (for more information on the effect of α, see Ref. 8). Also, the wake blockage effect, which can be related to the pressure coefficient values behind the model, at the right-hand side of this figure, is clearly increasing for the larger blockage ratios (blockage ratios are shown in the parentheses). It is interesting to compare the wing-induced pressure signature in this figure with the one in Fig. 2. There, the pressure coefficient does not recover to a value close to zero behind the models as it does in the case of the wings in Fig. 3. This, of course, is a result of the massive separated wake behind the cylindrical body, whereas with the wings the wake blockage effects on the ceiling pressures are much smaller.

The effect of the blockage ratio (or model size) on the lift and drag curve of the four wings is shown in Fig. 4. Again, as model size increases, the magnitude of the uncorrected aerodynamic coefficients increases. Because of the physical size of the larger wings, their angle of attack was limited to 14 deg, and only the smallest wing could be pitched up to 16 deg. Therefore, at the larger angles of attack the wing's leading edges were quite close to the ceiling, but in these experiments no effort was made to investigate the effect of wall proximity on wing stall. The value of the lift coefficients in this figure are somewhat less than the classical two-dimensional values presented in Ref. 9. This is a result of the wing side edges not being completely sealed against the tunnel side walls (by the foam seals at the tips), thus creating a small finite AR effect. The drag coefficient follows similar trends, but the magnitude of the changes was much smaller, as seen in Fig. 4. Also, the drag data had less separation because the measured loads were closer to the accuracy margin of the balance ($\Delta C_D = \pm 0.01$).

Concluding Remarks

The basic fact that a model in a wind tunnel is confined within limited boundaries will always have an effect on the flowfield. As the blockage ratio increases, wall interference effects may become quite large. The important finding here, however, is that the changes in the aerodynamic coefficients with increasing test-section blockage are gradual and monotonic and an engineering estimation of the necessary corrections is possible. The wall-pressure distribution signature varies in a similar manner and most likely can be used for engineering corrections, even when the blockage ratio reaches levels of 20%.

Acknowledgments

The participation and support of Steven Yon during the wind-tunnel experiments supporting this study are gratefully acknowledged.

References

[1]Pankhurst, R. C., and Holder, D. W., "Wind-Tunnel Technique," Pitman & Sons, Ltd., London, 1952.

[2]Rae, W. H., Jr., and Pope, A., "Low-Speed Wind Tunnel Testing," Wiley, New York, 1984.

[3]Garner, H. C., Rogers, E. W. E., Acum, W. E. A., and Maskell, E. C., "Subsonic Wind Tunnel Wall Corrections," AGARDograph 109, Oct. 1966.

[4]Hackett, J. E., Sampath, S., and Phillips, C. G., "Determination of Wind Tunnel Constraint Effects by a Unified Wall Pressure Signature Method," NASA CR-166, 186, June 1981.

[5]Ashill, P. R., and Keating, R. F. A., "Calculation of Tunnel Wall Interference from Wall-Pressure Measurements," *Aeronautical Journal*, Vol. 92, No. 911, 1988, pp. 36–52.

[6]Katz, J., "Integration of Computational Methods into Automotive Wind Tunnel Testing," Society of Automotive Engineers Paper 89-0601, Detroit, MI, Feb. 1989.

[7]Browne, L., and Katz, J., "Application of Panel Methods to Wind Tunnel Wall Interference Corrections," AIAA Paper 90-0007, Jan. 1990.

[8]Katz, J., and Walters, R., "Investigation of Wind-Tunnel Wall Effects in High Blockage Testing," AIAA Paper 95-0438, Jan. 1995.

[9]Abbott, I. H., and Von Doenhoff, A. E., "Theory of Wing Sections," Dover, New York, 1959, pp. 578, 579.

Unstructured Euler Flutter Analysis of Two-Dimensional Wing–Tail Configuration

Dartzi Pan* and Jen-Chieh Cheng†
National Cheng Kung University, Tainan 70101, Taiwan, Republic of China

Introduction

THE unsteady interferences from vortical disturbances in the flow can be important for the aeroelastic behavior of lifting surfaces. Frequently, these interferences alter the flowfield significantly, with consequent changes in aerodynamic loading and aeroelastic behavior of the lifting surfaces. In transonic regime where shock wave strength and position are sensitive to small changes in flow parameters, vortical wakes may be shed from the wing for a variety of flow conditions. The downstream tail is under the direct influence of such vortical wakes and may experience significant changes in aeroelastic characteristics. It is thus of practical importance to investigate the aerodynamic interferences and aeroelastic characteristics of the tail, under the influence of a stationary or oscillating forewing.

Most of the aeroelastic studies in the literature focus on the flutter behavior of an isolated airfoil. There have been few concerns about the aeroelastic characteristics of two-airfoil systems, which are the two-dimensional representation of a canard–wing or wing–tail configuration. Shankar and Malmuth[1] performed the steady transonic small disturbance calculations for the two-dimensional canard–wing systems. Batina[2] studied the aeroelastic stability and flutter of two-dimensional wing–canard configurations in frequency domain. These studies are all based on the transonic small disturbance equations, where the shock is weak and the airfoil motion is assumed small. Recently, the Euler solver on dynamic unstructured meshes are employed for more realistic aeroelastic studies. For example, Rausch et al.[3] performed the Euler flutter analysis of airfoils using unstructured dynamic meshes. Batina[4] calculated the unsteady flow over an aircraft oscillating with a fuselage bending mode. The Euler solvers in these studies are based on multistage Runge–Kutta time-stepping schemes with added artificial dissipation terms to control the stability and the oscillation across solution discontinuities.

Received May 20, 1993; presented as Paper 94-0284 at the AIAA 32nd Aerospace Sciences Meeting and Exhibit, Reno, NV, Jan. 10–13, 1994; revision received Jan. 15, 1995; accepted for publication March 15, 1995.

*Associate Professor, Institute of Aeronautics and Astronautics. Member AIAA.

†Graduate Student, Institute of Aeronautics and Astronautics.

Euler Solver on Dynamic Unstructured Mesh

In this study, an upwind unstructured Euler solver based on Roe's approximate Riemann solver[5,6] and a two-degree-of-freedom aeroelastic solver are employed for the time-domain flutter analysis of wing–tail configurations. A dynamic grid method is implemented by treating the mesh as a spring network where each edge of each cell represents a spring with stiffness inversely proportional to the length of that edge. The outer boundary of the mesh is held fixed in space, while the inner boundaries such as the surfaces of the wing and the tail are allowed to move in a prescribed manner or as determined by aeroelastic solver. The positions of the interior nodes are then determined by the static equilibrium of the spring system. The geometrical conservation laws (GCL) are enforced by the procedure proposed by Vinokur,[7] which avoids the explicit integration of the cell volume.

Time-Marching Aeroelastic Solver

The aeroelastic solver takes the aerodynamic loads computed by the Euler solver as the input forcing functions. It then solves the classical aeroelastic equations of motion for a typical section airfoil in terms of plunge and pitch degree of freedom. Considering the inertia, elastic, and aerodynamic forces, the nondimensional aeroelastic equations of motion without damping can be written as

$$M\ddot{y} + Ky = Gu \tag{1}$$

where $y = [h\alpha]^T$ is the vector of plunge displacement h (positive when downward) and pitch displacement α (positive when nose-up) measured from the assumed static operating condition; $u = [(C_L - C_{L0})(C_M - C_{M0})]^T$ is the vector of aerodynamic loads with the static load C_{L0} and C_{M0} subtracted; and matrices M, K, and G are the coefficient matrices of generalized mass, stiffness, and forces, respectively. In particular, a speed index $V^* = 2U_\infty/c\omega_\alpha$ is involved in matrix K, where c is the chord length and ω_α is the uncoupled natural frequency in pitching. It is convenient to put Eq. (1) in a linear state equation form:

$$\dot{x} = Ax + Bu \tag{2}$$

where $x = [h\alpha\dot{h}\dot{\alpha}]^T$ and matrices A and B are made of M, K, and G. After approximations for a small time step, Eq. (2) is integrated in time by the algorithm of Edwards et al.[8]:

$$x_{n+1} = \Phi x_n + \Theta B(3u_n - u_{n-1})/2 \tag{3}$$

where Φ is the state-transition matrix, and Θ is the integral of Φ from time step n to $n + 1$. By varying V^*, the time history of displacement is recorded and processed by a fast Fourier transform (FFT) analysis or a modal identification technique by Bennert and Desmarais[9] to identify its damping and frequency. The system is said to be fluttering when the system damping is negative.